

Fast Image Dehazing Method Based on Linear Transformation

Wencheng Wang, Xiaohui Yuan, *Member, IEEE*, Xiaojin Wu and Yunlong Liu

Abstract—Images captured in hazy or foggy weather conditions are seriously degraded by the scattering of atmospheric particles, which directly influences the performance of outdoor computer vision systems. In this paper, a fast algorithm for single image dehazing is proposed based on linear transformation by assuming that a linear relationship exists in the minimum channel between the hazy image and the haze-free image. First, the principle of linear transformation is analyzed. Accordingly, the method of estimating a medium transmission map is detailed and the weakening strategies are introduced to solve the problem of the brightest areas of distortion. To accurately estimate the atmospheric light, an additional channel method is proposed based on quad-tree subdivision. In this method, average grays and gradients in the region are employed as assessment criteria. Finally, the haze-free image is obtained using the atmospheric scattering model. Numerous experimental results show that this algorithm can clearly and naturally recover the image, especially at the edges of sudden changes in the depth of field. It can thus achieve a good effect for single image dehazing. Furthermore, the algorithmic time complexity is a linear function of the image size. This has obvious advantages in running time by guaranteeing a balance between the running speed and the processing effect.

Index Terms—Dehazing, linear transformation, image restoration, transmission map.

I. INTRODUCTION

Accurate extraction of image features is a key factor that directly influences the performance of computer vision systems [1]. However, in hazy or foggy weather conditions, image quality severely degrades due to light scattering by atmospheric particles, and many characteristics of the hazy image are covered. Therefore, improving image quality and enhancing system robustness in challenging weather conditions has important scientific significance and broad application values. Its research results can be widely used in urban transportation [2], outdoor video surveillance [3], driver assistance systems [4], and satellite remote sensing [5]. In addition, they provide reference values for underwater image analysis [6] and rainy and snowy image processing fields.

Currently, existing image dehazing methods can be divided into two categories: image enhancement-based methods and

image restoration-based methods.

Image enhancement-based methods include histogram equalization [7,8], the Retinex method [9], homogeneous filtering [10], wavelet transformation [11], and others. Histogram equalization enhances the overall contrast of a hazy image by increasing the dynamic range of the gray values [7]. However, the global histogram equalization (GHE) has difficulty restoring the optimal value for each local area, whereas local histogram equalization (LHE) has a large complexity of computation. The Retinex method can effectively maintain the balance between the color constancy and dynamic range compression [9]. However, it does not have an edge-preserving ability, which results in halo phenomena in some sharp boundary regions. The goal of homogeneous filtering [10] is to combine frequency filtering and grayscale transformation to improve image quality. It can effectively retain the contour information in uneven regions. However, its computation burden is notable. Wavelet transform (WT) [11] improves image quality by dehazing low-frequency regions and enhancing high-frequency regions. Nevertheless, this approach has difficulty resolving over-brightness and uneven illumination issues. In short, the main purpose of hazy image enhancement is to satisfy the visual perception of the human eye and provide greater convenience for computer recognition without considering the degradation model.

Since 1998, Oakley et al. [12] began using the atmospheric scattering law for research on images obtained in bad weather. Narasimhan et al. [13] proposed a single hazy image interactive restoration method. It must artificially specify the maximum and minimum depths of field areas to obtain rough depth information. Hautiere et al. [14] estimated visibility distance through an onboard optical sensor system to compute the scene depth. They employed a 3D geographical model to remove the haze. In addition, Kopf et al. [15] used existing geo-referenced digital terrain to provide basic information. They then built a 3D model of the scene with a large amount of depth information to achieve dehazing. This kind of method is based on the premise that the scene depth is known, which severely limits the application of this algorithm in a real-time system. In contrast to this, Schechner et al. [16,17] studied the polarization characteristics of light and captured the same scene images with different polarization angles to obtain the depth information, and then restored the degraded image. Narasimhan and Nayar [18-20] proposed another approach to obtain scene depth information by capturing two of the same scene images under different weather conditions. This type of dehazing method can achieve good results while it is difficult to capture images.

In recent years, some single image dehazing methods based on additional priors or constraints have been proposed. For example, Tan [21] proposed an effective method based on the prior that the contrast in a fogless image is higher than that of a foggy image and then realized the dehazing by maximizing the

This work was supported by the National Natural Science Foundation of China (Grant No. 61403283), Shandong Provincial Natural Science Foundation (No. ZR2013FQ036, ZR2015PE025), the Spark Program of China (No. 2013XH06034), the Spark Program of Shandong Province (No. 2013XH06034) and Technology Development Plan of Weifang City (No. 201301015).

Wencheng Wang, Xiaojin Wu, and Yunlong Liu are with the College of Information and Control Engineering, Weifang University, Weifang, 261061 China (e-mail: wwwcfu@126.com, wfuwxj@163.com, fhylren@163.com). Wencheng Wang is currently also a visiting scholar at the University of North Texas, Denton, TX.

Xiaohui Yuan is with Department of Science and Engineering, University of North Texas, Denton, TX, 76207 USA (e-mail: xiaohui.yuan@unt.edu).

local contrast with only one image. However, in this approach, color can easily become oversaturated in a heavily hazy image. Fattal [22] used independent component analysis (ICA) and the Markov random field (MRF) model to estimate the surface albedo based on the prior knowledge that no correlation exists between the object surface shading and the transmission map; however, it may fail in cases where this assumption is invalid. Later, the author [23] presented another method based on the color-lines pixel regularity in natural images in order to resolve the transmission better in isolated pixels that are lacking their own estimates. Kratz and Nishino [24] proposed a method related to the Tan solution [21]. This approach can recover a haze-free image with fine edge details; however, the results tend to be overly enhanced and suffer from oversaturation. Later, they introduced a novel Bayesian probabilistic method [25] to estimate the scene albedo and depth by fully leveraging their latent statistical structures. Nevertheless, this technique produces some dark artifacts in regions that approach infinite depth. In addition, He et al. [26] presented an effective method based on the dark channel prior (DCP). In this approach, minimum filtering is used to estimate a rough transmission map, and soft matting is adopted to refine the rough transmission map to produce better performance. However, due to the soft matting, the algorithm has high computational complexity. Other approaches, such as bilateral filtering [27], median filtering [28,29], edge-preserving filtering [30], and guided filtering [31], are used to optimize the transmission to enhance the algorithm performance. Tarel et al. [32] introduced a contrast-based enhancing approach to remove the haze effects that was aimed at being faster than the previous approaches. It is assumed that the atmospheric veil function changed gently in the local region, so the transmission coefficient of the medium can be estimated by pretreatment and median filtering, which greatly simplifies the dehazing process and improves the efficiency. Nevertheless, many parameters in the algorithm cannot be adaptively adjusted. To retain the balance of overstretched contrast, Kim et al. [33] optimized contrast enhancement by maximizing the blockwise contrast, while minimizing information loss due to pixel truncation. Furthermore, Meng et al. [34] provided a transmission image optimization algorithm by exploring boundary constraint and contextual regularization. This method can attenuate image noise and enhance some interesting image structures. Ancuti et al. [35] demonstrated the utility and effectiveness of a fusion-based technique for dehazing on a single degraded image. These inputs from a hazy image are weighted by three normalized weight maps and finally blended in a multi-scale manner that avoids artifact introduction [36]. In addition, Zhu et al. [37] proposed a color attenuation prior to create a linear model for the scene depth of a hazy image. Their approach employs a supervised learning method and utilizes the recovered depth information, thereby making it easy to remove the haze from a single hazy image.

Although the above dehazing methods can achieve good results on a single image, the high computation limits their applications in real-time systems[38]. To maintain the balance between efficiency and speed, a fast image restoration-based method is proposed by assuming that a linear relationship exists in the minimum channel between the hazy image and the

haze-free one. In this method, the transmission map is estimated using a linear transformation model which has less computational complexity, and the atmospheric light is obtained with an additional channel method based on a quad-tree subdivision by using the ratio of grays and gradients in the region. With those information, we can easily get the haze-free image through the atmospheric scattering model.

The remainder of this paper is organized as follows. In Section 2, the atmospheric scattering model is introduced. The image dehazing algorithm based on linear transformation is described in Section 3. Moreover, the method for estimating the transmission map, along with the key steps in the estimation of the atmospheric light, are described. In Section 4, the experimental results are presented for comparison with those of other methods. Our conclusions are provided in Section 5.

II. ATMOSPHERIC SCATTERING MODEL

According to the atmospheric scattering theory, the scattering of atmospheric particles is mainly divided into two parts: one is the attenuation process of reflected light from the object surface to the camera; the other is the scattering of airlight reaching the camera [39]. A schematic diagram of the atmospheric scattering model is shown in Fig. 1. The solid line denotes light from the object to the camera; the dotted line represents airlight.

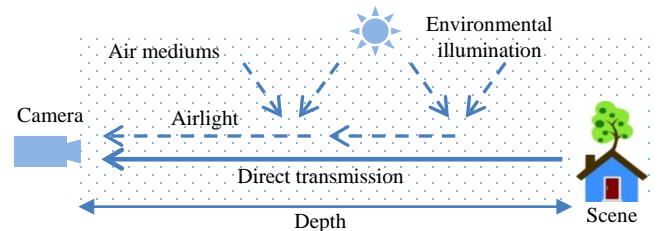


Fig. 1. Atmospheric scattering model.

In computer vision and computer graphics, the scattering model of a hazy image can be expressed as:

$$E(d, \lambda) = E_0(\lambda)e^{-\beta(\lambda)d} + E_\infty(\lambda)(1 - e^{-\beta(\lambda)d}) \quad (1)$$

where λ is the wavelength of visible light, d is the distance from scene to camera, $\beta(\lambda)$ is the atmospheric scattering coefficient, and $E_0(\lambda)$ and $E_\infty(\lambda)$ are the radiation intensity at $x=0$ and $x=\infty$, respectively.

This kind of dehazing method serves to remove the effect of atmospheric light in order to restore the details of the image and color information. Let $I(x) = E(d, \lambda)$, $J(x) = E_0(\lambda)$, $t(x) = e^{-\beta(\lambda)d}$, $A = E_\infty(\lambda)$, Eq.(1) can be simplified to:

$$I(x) = J(x)t(x) + A(1 - t(x)) \quad (2)$$

where x is the coordinates, $I(x)$ is hazy image, $J(x)$ is the haze-free image, A is the atmospheric light, and $t(x)$ is the medium transmission map.

As shown by Eq.(2), the main difficulty in solving single image dehazing is the double unknowns of the haze-free image $J(x)$, and the transmission map $t(x)$, which is severely ill-posed. However, if the depth information of an image is known or if we have some prior knowledge for the single image, then $J(x)$ can still be resolved.

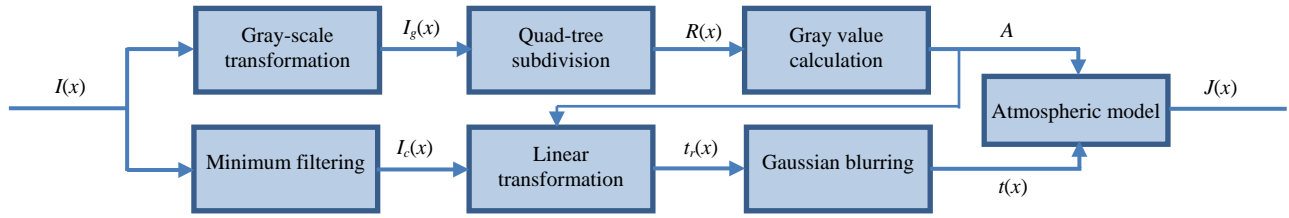


Fig. 2. The flow chart of proposed method

III. DEHAZING METHOD BASED ON LINEAR TRANSFORMATION

The flow chart of the proposed method is shown in Fig. 2, which is divided into three steps according to the atmospheric scattering model. (1) Atmospheric light estimation is performed through grayscale transformation to find $I_g(x)$. Then, the quad-tree subdivision is adopted to obtain the sky region, $R(x)$, and finally, the atmospheric light A is obtained by calculating the average gray of the sky region. (2) A transmission map is estimated by calculating the minimum color channel of $I(x)$ to obtain $I_c(x)$. Then, the linear transformation algorithm is used to estimate the rough transmission map, $t_r(x)$, and finally, the Gaussian blur method is used to refine the rough transmittance function to obtain $t(x)$. (3) Image restoration with parameters $t(x)$ and A is used to recover the haze-free image based on the atmospheric scattering model.

A. Transmission Map Estimation

(1) Linear transformation

The effect of atmospheric light on imaging increases as the distance from the scene to the observation point increases, and from the visual effect, the brightness of the image is gradually increased as the fog thickens. To estimate the medium transmission map, Eq.(2) can be transformed into:

$$t(x) = \frac{A - I(x)}{A - J(x)} \quad (3)$$

In color images, since at least one reflection coefficient of the color component is very small, the numerator and denominator were calculated for three color channels with minimum filter, giving:

$$t(x) = \frac{\min_{c \in \{r,g,b\}} A^c - \min_{c \in \{r,g,b\}} I^c(x)}{\min_{c \in \{r,g,b\}} A^c - \min_{c \in \{r,g,b\}} J^c(x)} \quad (4)$$

where c is the color channel of the hazy image, $c \in \{r, g, b\}$, $I^c(x)$ is the c channel value at pixel x of I . Suppose the atmospheric light A is the vector with the value $\{A_0, A_0, A_0\}$, then Eq.(4) will change to:

$$t(x) = \frac{A_0 - \min_{c \in \{r,g,b\}} I^c(x)}{A_0 - \min_{c \in \{r,g,b\}} J^c(x)} \quad (5)$$

Because the transmission rate is related to the distance under hazy conditions, the larger imaging distance, the higher the pixel value on the image. Therefore, suppose in the imaging process, the minimum color component of the three channel increases linearly as the transmission rate increases, which is:

$$\min_{c \in \{r,g,b\}} J^c(x) \propto \min_{c \in \{r,g,b\}} I^c(x) \quad (6)$$

Then, the above equation will be expressed as:

$$\min_{c \in \{r,g,b\}} I^c(x) = a \times \min_{c \in \{r,g,b\}} J^c(x) + b \quad (7)$$

where a is the slope and b is the intercept. However, the addition of two unknown parameters makes the equation more difficult. Therefore, it is altered so that it is approximately expressed using the piecewise region of a quadratic function:

$$\min_{c \in \{r,g,b\}} J^c(x) = \frac{\min_{c \in \{r,g,b\}} I^c(x) - \text{Min}}{\text{Max} - \text{Min}} \times \min_{c \in \{r,g,b\}} I^c(x) \quad (8)$$

where Max and Min are the maximum and minimum of

$\min_{c \in \{r,g,b\}} I^c(x)$, respectively. Thus, $0 \leq \frac{\min_{c \in \{r,g,b\}} I^c(x) - \text{Min}}{\text{Max} - \text{Min}} \leq 1$.

Take $i = \min_{c \in \{r,g,b\}} I^c(x)$ as the independent variable on the

horizontal axis, and take $j = \min_{c \in \{r,g,b\}} J^c(x)$ as the dependent

variable on the vertical axis. The relationship curve between them is shown in Fig. 3.

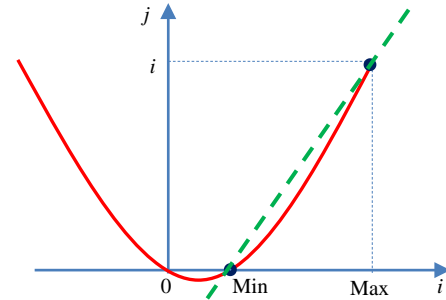


Fig. 3. Curve of j changes with i

Therefore, in the range of $[\text{Min}, \text{Max}]$, the linear relationship of the piecewise function in the red solid curve can be approximated by the green straight line in the graph. When $i = \text{Min}$, then $j = 0$; when $i = \text{Max}$, then $j = i$.

A control factor, δ , is introduced into the expression to constrain the speed of the linear change. Hence, Eq.(8) is changed to:

$$\min_{c \in \{r,g,b\}} J^c(x) = \delta \times \frac{\min_{c \in \{r,g,b\}} I^c(x) - \text{Min}}{\text{Max} - \text{Min}} \times \min_{c \in \{r,g,b\}} I^c(x) \quad (9)$$

where $0 \leq \delta \leq 1$. The variation of the curvature for different δ is shown in Fig. 4, where the green curve, blue curve and red curve correspond to $\delta=0.7$, $\delta=0.85$, and $\delta=1$, respectively.

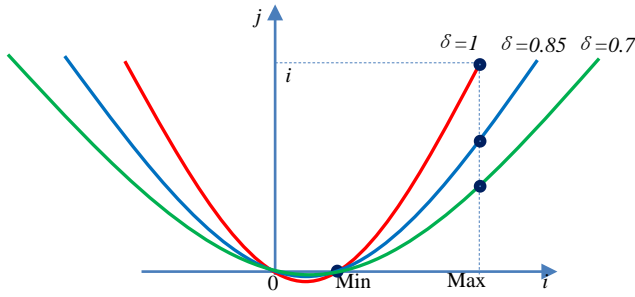


Fig. 4. Curves of j changes with i under different δ .

As seen from Fig. 4, as δ decreases, the variation speed of $\min_{c \in \{r,g,b\}} J^c(x)$ with $\min_{c \in \{r,g,b\}} I^c(x)$ decreases. In summary, Eq.(3) can be expressed as follows:

$$t(x) = \frac{A_0 - \min_{c \in \{r,g,b\}} I^c(x)}{A_0 - \delta \times \frac{\min_{c \in \{r,g,b\}} I^c(x) - \min_{c \in \{r,g,b\}} (\min_{c \in \{r,g,b\}} I^c(x))}{\max_{c \in \{r,g,b\}} (\min_{c \in \{r,g,b\}} I^c(x)) - \min_{c \in \{r,g,b\}} (\min_{c \in \{r,g,b\}} I^c(x))}} \times \min_{c \in \{r,g,b\}} I^c(x) \quad (10)$$

As shown by the above formula, $I(x)$ is known. As long as the value of A_0 is known, then the whole image transmission map will be obtained accordingly. Based on this formula, when δ decreases, the obtained transmission maps and the restored images are as shown in Fig. 5, where Fig. 5 (a) is the hazy image and the first row and second row of Fig. 5 (b) - (e) are the transmission maps and haze-free images corresponding to different δ from 1 to 0.4, respectively.

Fig. 5 shows that as δ decreases, the contrast of the transmission map increases and the degree of dehazing is enhanced accordingly.

(2) Processing of the brightest region

In Eq.(9), the numerator is always greater than the denominator; therefore, $t(x) \leq 1$. If $\min_{c \in \{r,g,b\}} I^c(x) \leq A_0$ (that is, atmospheric light is the brightest region), then $0 \leq t(x) \leq 1$. Otherwise, when $\min_{c \in \{r,g,b\}} I^c(x) \geq A_0$, $t(x) \leq 0$, which is unreasonable for the assumption that $0 \leq t(x) \leq 1$.

In Eq.(10), suppose $\max_{c \in \{r,g,b\}} (\min_{c \in \{r,g,b\}} I^c(x)) = 0.95$, $A_0 = 0.9$, and $\min_{c \in \{r,g,b\}} (\min_{c \in \{r,g,b\}} I^c(x)) = 0.05$. Then, the curves of the transmission rate $t = t(x)$ vary with $i = \min_{c \in \{r,g,b\}} I^c(x)$, as shown in Fig. 6(a). As $\min_{c \in \{r,g,b\}} I^c(x)$ increases, $t(x)$ gradually decreases; moreover, when $\min_{c \in \{r,g,b\}} I^c(x) \geq A_0$, $t(x)$ becomes

negative. The common operation is $\max(t(x), 0)$; that is, negative values are set as 0, as shown in Fig. 6(b). However, this will lead to the over-processing of the brightest regions.

To avoid this situation, the absolute value calculation is used to obtain a positive value when the high brightness pixels are greater than the atmospheric light. The brightness value is higher than that of atmospheric light. Furthermore, the impact degree from the haze is smaller. Thus, the higher the transmission rate that can be set, the smaller the error. The variation curve is shown in Fig. 6(c), where the red, green, blue, and black curves relate to different δ . As δ increases, in the region of $\text{Max} \geq \min_{c \in \{r,g,b\}} I^c(x) \geq A_0$, $t(x)$ changes faster. As

shown in Fig. 6(d), when $\delta = 0.93$, at the horizontal axis of $\min_{c \in \{r,g,b\}} I^c(x) = \text{max}$, the output $t(x)$ reaches 3. Although it

can be processed with $\min(t(x), 1)$ —that is, the values are set to be greater than 1—this will ignore the difference in the brightness values. Thus, we adopt the normalization method to address this kind of situation with the normalized coefficient $1/t(\text{Max})$. Then, Eq.(10) is changed to:

$$t'(x) = \begin{cases} |t(x)| & \min_{c \in \{r,g,b\}} I^c(x) \geq A_0 \\ \frac{1}{\max(t(\text{Max}), 1)} \times |t(x)| & \min_{c \in \{r,g,b\}} I^c(x) < A_0 \end{cases} \quad (11)$$

This process can ensure the continuity of the medium transmission rate in the regions that are too bright.

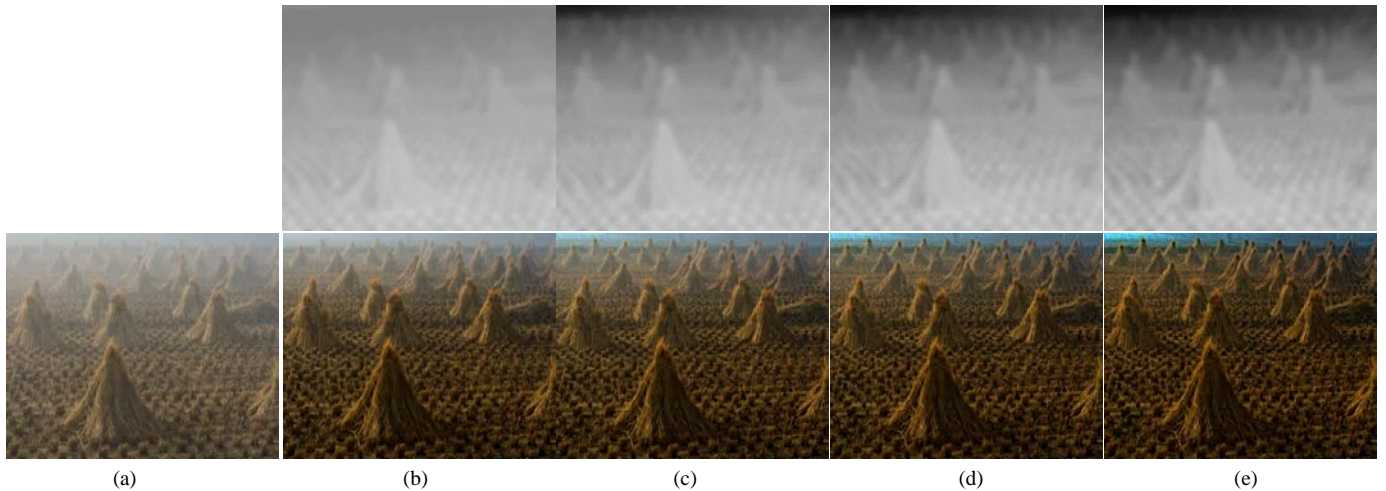


Fig. 5. Transmission map and restored image with different δ . (a) Original image. (b) $\delta = 1.0$. (c) $\delta = 0.8$. (d) $\delta = 0.6$. (e) $\delta = 0.4$.

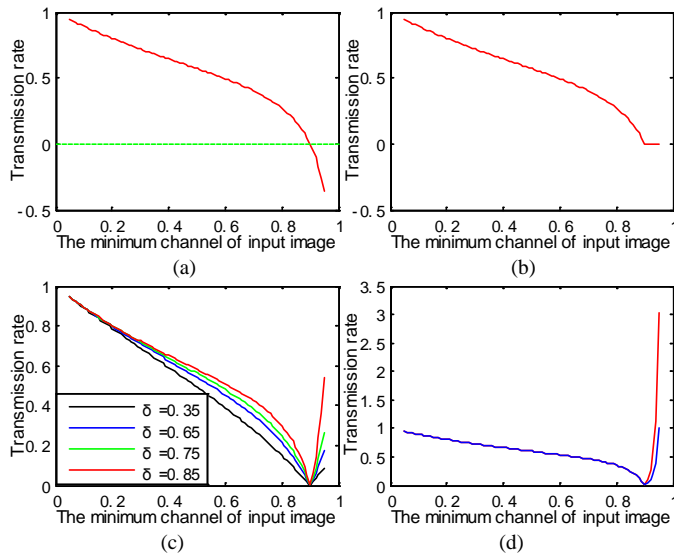


Fig. 6. Processing on bright region. (a) Negatives of $t(x)$. (b) Negatives replaced with 0. (c) Variation of $t(x)$ with different δ . (d) Normalization processing.

(3) Gaussian blur

The transmission rate obtained via the above method is pixel-based, which is greatly influenced by its own grayscale value. Considering that the transmission rate changes slowly in a certain area, it is necessary to carry out a smoothing operation to improve the visual effect. The simple average filtering is obviously unreasonable because it does not take the weight into account and causes the edges to blur. This means that the closer the relationship is between adjacent pixels, the higher the weights should be. Otherwise, the weight should be lower. Therefore, the weighted average method should be used. The Gaussian blur method is used only to replace each pixel value by the weighted average value of all pixels in the pixel neighborhood. It has isotropic and homogeneous properties. With the template size $M \times N$, the Gaussian function of elements (x, y) can be expressed as:

$$G(x, y) = \frac{1}{2\pi\sigma^2} e^{-\frac{(x-m/2)^2 + (y-n/2)^2}{2\sigma^2}} \quad (12)$$

where σ is the standard deviation of the normal distribution values; the greater the σ , the more blurred the images. Then,

after convolution of two non-null matrixes, the filtered distribution map can be obtained. It is expressed as:

$$t''(x) = t'(x) * G \quad (13)$$

where $*$ represents the convolution operation and G is the Gaussian window. Each pixel value is the weighted average of the original pixel and its neighbors, which can yield a more effective edge-preserving effect than average smoothing.

In addition to the above method, other approaches can be used for image smoothing. Fig. 7 shows the processing results with the different methods, where Fig. 7(a) is the hazy image and Fig. 7(b)-(h) are the restored images whose transmission maps are processed with non-filtering, average filtering, median filtering, Gaussian filtering, recursive bilateral filtering, anisotropic filtering, and guided filtering, respectively.

According to the above experimental results, the filtered transmission map is smoother from the visual effects, while the recovered image is more realistic. In the recovered image, the effects of using a Gauss filter, anisotropic filter, and guided filter are better than those from the average filter, median filter, and bilateral filter. The required times for the above filtering methods to address a 600×400 pixel image in the MATLAB environment are shown in Table 1.

Tab. 1 The running time comparison with different filters

Methods	Gaussian filtering	Average filtering	Recursive bilateral filtering	Anisotropic filtering	Median filtering	Guided filtering
Time (s)	0.021	0.016	0.039	0.530	0.048	0.097

Based on the above results, considering both the effect and efficiency of the operation, adopting the Gaussian blur method for transmission map smoothing is reasonable. In practice, the filter window is set to 15×15 pixels.

B. Atmospheric Light Estimation

Another key factor for solving Eq.(10) is the estimation of the atmospheric light A_0 , which is important in image dehazing [40]. According to its own haze characteristics, a large amount of haze will increase the brightness of an object in an image. In Tan's work [21], the brightest pixels in a hazy image are used as the atmospheric light. Additionally, He et al. [26] used the pixels with the highest intensity in hazy images. Then, the top 0.1% of the brightest pixels were selected in the

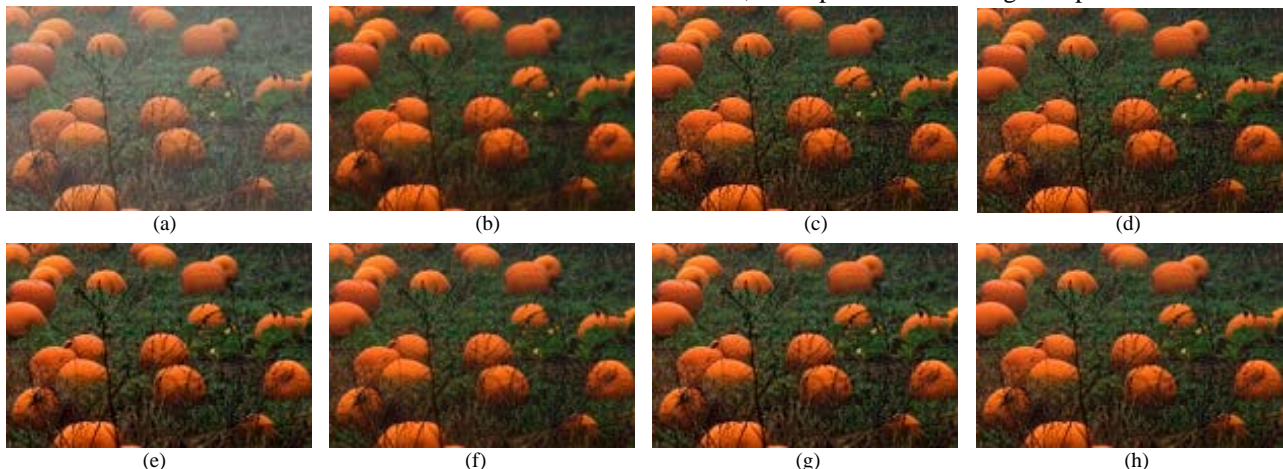


Fig. 7. Effects of different filters on the transmission map. (a) Hazy image. (b) Without filtering. (c) Average filtering. (d) Median filtering. (e) Gaussian filtering. (f) Recursive bilateral filtering. (g) Anisotropic filtering. (h) Guided filtering.

dark channel. However, the above two methods were influenced by white objects.

Kim et al. [33] selected the atmospheric light in a hazy image using a hierarchical searching method based on the quad-tree subdivision. In this approach, an image is repeatedly divided into four rectangular regions. The brightest region is chosen as atmospheric light according to the threshold. This method is reliable; however, it employs only the average gray as the criteria and results in white regions. Fig. 8(a) and (b) are images named ‘the forbidden palace’ and ‘Lake,’ respectively. The black regions are the final selection result based on Kim’s method [33]. The expected sky regions are located on the stone and water surfaces, respectively, due to the interference of white regions.

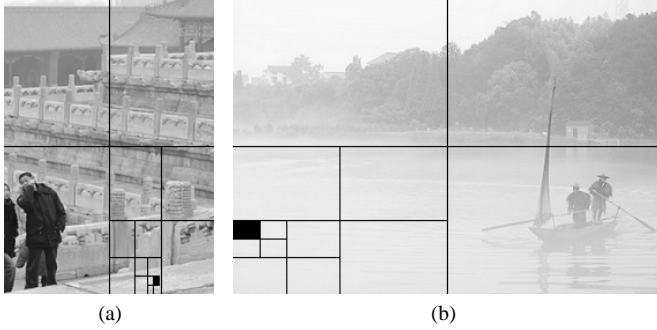


Fig. 8. The sky region location using quad-tree subdivision [33]. (a) Quad-tree of ‘the forbidden palace’. (b) Quad-tree of ‘Lake’.

To improve the positioning accuracy and robustness, an additional channel method is proposed based on quad-tree subdivision; this method is based on the experience knowledge that the sky areas are mainly distributed in the middle or upper parts of images. First, the hazy color image is transformed to a gray image, and then, the image is divided into four parts x_n^i , $i \in [1,2,3,4]$ represents the regions of upper left, upper right, bottom left and bottom right, respectively. In addition, n is the level of subdivision, where $n=1$ represents the first subdivision on the source image. The average gray value of each region $S(x_n^i)$ is defined as the score of this region x_n^i , and the formula is expressed as:

$$S(x_n^i) = \text{mean}(I(x_n^i)) \quad (14)$$

If the highest score region of the first subdivision is on the upper-half of the image, i.e., $\max(S(x_1^i)) \in [S(x_1^1) | S(x_1^2)]$, then this region will be the new area that is divided into four smaller blocks using the quad-tree method for the next iterative step. Eq.(14) is used to iteratively calculate the score until the selected area is less than a predefined termination threshold. Thus, the final region x_{final} is obtained. However, if the highest score region of the first subdivision is on the bottom-half (x_1^3 or x_1^4) of the image, then the upper-half regions (x_1^1 or x_1^2) will be calculated with a weight coefficient η . Then, the scores of $\{\eta \times S(x_1^1), \eta \times S(x_1^2), S(x_1^3), S(x_1^4)\}$ are compared, and the region with the highest score is selected for the next subdivision. If the region is still on the bottom-half (x_1^3 or x_1^4) of the image, then this region will be the new area that is iteratively processed using the quad-tree method until the

final region x_{final} is obtained. Otherwise, except to obtain candidate x_{final} , the new highest score region on the upper-half part (x_1^1 or x_1^2) of the image will be subdivided to obtain another candidate final region x'_{final} , which is called the additional channel.

There is an absolute termination condition in the above quad-tree subdivision process; that is, if the difference between the maximum average gray value and the second highest average gray value is less than S_T , then the region with the highest score will not be divided further without considering whether it reached the setting size. Assuming that in the n^{th} level subdivision, the maximum score is $S(x_n^k)$, then the absolute termination rule is:

$$\min |S(x_n^k) - S_n(x_n^{\bar{k}})| \leq S_T \quad (15)$$

where \min is the minimum operation and \bar{k} is the remaining regions of region k . If the above procedure may generate two candidate regions of x_{final} and x'_{final} , then the two regions will be compared based on the ratio between the average gray and the average gradient of each region, which can be expressed as:

$$S'(x_n^i) = \text{mean}_{\text{gray}}(I(x_n^i)) / \text{mean}_{\text{gradient}}(I(x_n^i)) \quad (16)$$

where $\text{mean}_{\text{gray}}$ is the average gray and $\text{mean}_{\text{gradient}}$ is the average gradient. Compare the $S'(x_{final})$ and $S'(x'_{final})$ of two regions, and select the larger one as the final sky region. Finally, the top 10% brightest pixels in the final region were selected, and the average gray value will be used as the atmospheric light value A_0 . The flow chart is shown in Fig. 9.

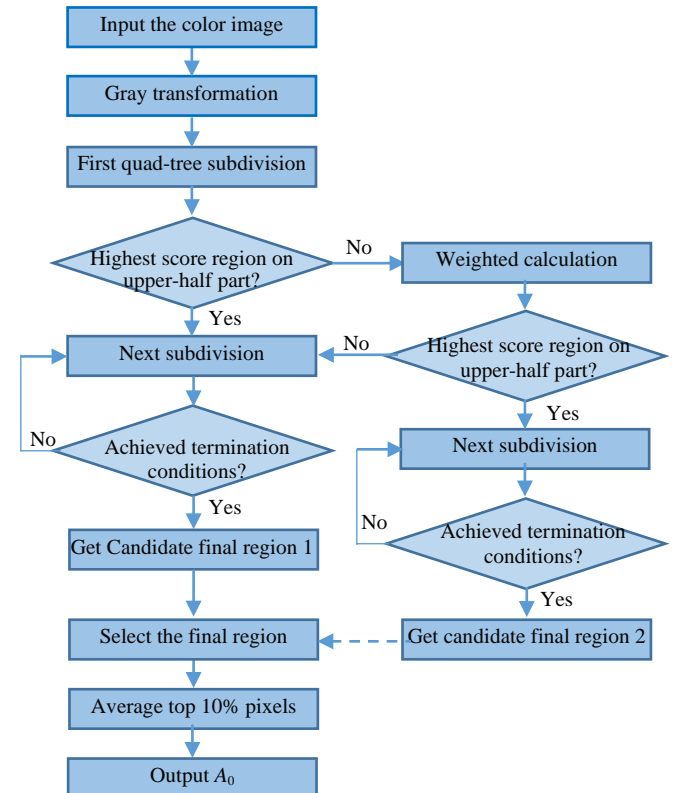


Fig. 9. Flowchart of the method for estimating atmospheric light.

Two examples using the above method are shown in Fig. 10.

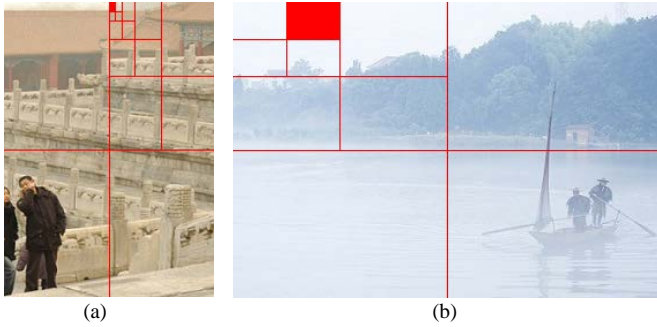


Fig. 10. Sky region positioning using the proposed method. Subdivision of 'the forbidden palace'. (b) Subdivision of 'Lake'.

Fig. 10 shows that the expected sky regions are positioned in the red-filled rectangle.

C. Haze-free image recovery

According to the atmospheric scattering model, once the transmission map $t(x)$ and atmospheric light A_0 are obtained, the scene radiance can be recovered with the following formula transformed from Eq.(2):

$$J(x) = \frac{I(x) - A_0}{\max(t(x), t_0)} + A_0 \quad (17)$$

where t_0 is a lower bound used for restricting the transmission map, which is set to 0.05. In addition, due to the influence of different ambient light on imaging, the brightness of some

images is low; after the recovery, the overall visual effect may be darker. Thus, the gray compensation method can be used to adjust the brightness according to the actual situation.

IV. ANALYSIS OF THE EXPERIMENTAL RESULTS

To test the performance of the proposed method, numerous experiments were conducted. All of the algorithms are implemented in the MATLAB R2014 environment on a DELL notebook computer with the processor i7-5500U @2.4 GHz with 8GB RAM. Hazy images for the experiments were classics in the field and selected from well-known literature sources. They cover city street scenes, natural scenery, aerial images, long-shot scenery, and close-shot scenery. Some of the experimental results are shown in Fig. 11, including a total of eight groups of experimental images with the names 'Hong Kong', 'House', 'Building', 'NewYork', 'Hill', 'Stadium', 'Trees', and 'Road'. For each group, the first row is the original hazy image, and the second is the haze-free image. The figure shows that using the proposed method, the images—regardless of whether they had marked or gentle changes of field depth or whether they were color or gray images—obtained restored results with natural color and clear details under all of the different conditions. This feasibility and effectiveness of the transmission map estimation shows that the method has strong robustness.



Fig. 11. Part of the experiment results of proposed method. (a) 'Hong Kong'. (b) 'House'. (c) 'Building'. (d) 'NewYork'. (e) 'Hill'. (f) 'Stadium'. (g) 'Trees'. (h) 'Road'.

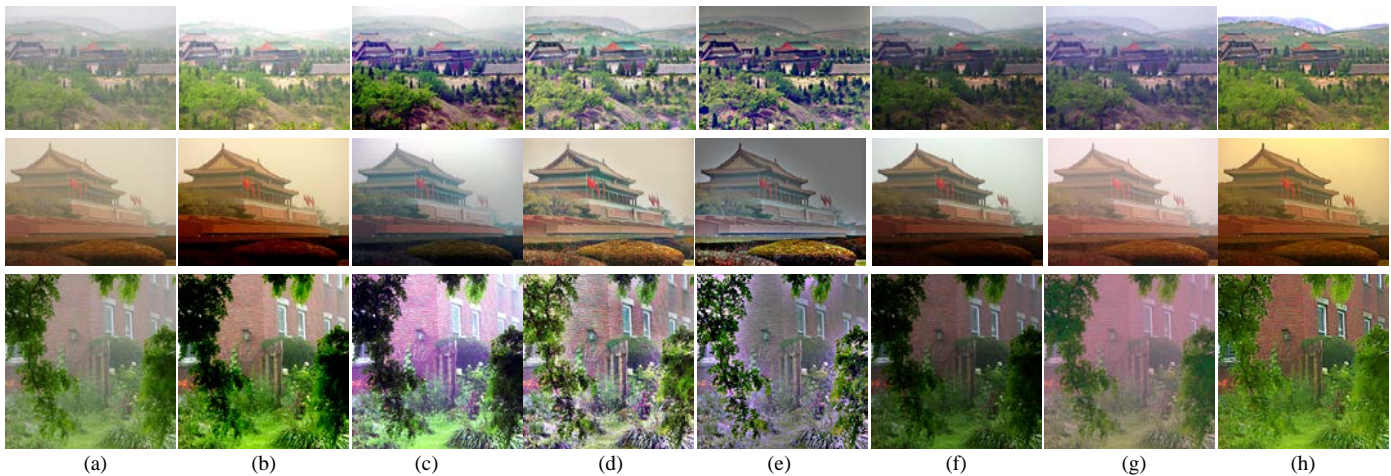


Fig. 12. Comparison between our proposed method and the traditional image enhancement methods. (a) Hazy image. (b) Grayscale stretching. (c) Histogram equalization. (d) Adaptive histogram equalization. (e) Retinex method. (f) Homomorphic filtering. (g) Wavelet transform. (h) Our method.

To reflect the reliability and advancement of the proposed method, the experimental results were compared with those of the other well-known methods on multiple images, such as classical image enhancement [7-11], Kopf's method [15], Tan's method [21], Fattal's method [22], He's method [26,31], Tarel's method [32], Nishino's method [25], Kim's method [33], Meng's method [34] and Zhu's method [37] with subjective evaluation, objective evaluation, and time complexity.

A. Subjective evaluation

(1) Comparison with image enhancement methods.

Fig. 12 shows a comparison of the experimental results between the proposed method and some image enhancement methods. Fig. 12(a) is the hazy image. Fig. 12(b)–(h) are the images processed with grayscale stretching, histogram equalization, adaptive histogram equalization, the Retinex method, homomorphic filtering, wavelet transform, and the proposed algorithm. As shown in Fig. 12(b)–(h), in the visual effects, all have different degrees of changes. In Fig. 12(c), (d), and (e), the image contrast is remarkably enhanced; the details become clearer with brighter color. However, in Fig. 12(g), the color tone significantly shifts and loses the true color of the original. Fig. 12(b) and (f) have minimal tone shifting overall; however, the improvement effect is still not ideal. In Fig. 12(b), the grayscale stretching results in the loss of some details. The edge of the mountain becomes vague. In Fig. 12(f), the homogenous filtering method results in a darker color with a lower contrast in the image. In contrast, the method proposed in this paper shows obvious improvements to the hazy image in both tone and detail recovery. The visual effect is obviously better than that of the above methods.

(2) Comparison with well-known image restoration methods.

The 'House' and 'Flag' images are used as the first group of experimental images; they are rich in edge information and depth information and frequently selected for comparison in literature studies. By adopting Kim's method [33], He's method [31], Tarel's method [32], Zhu's method [37] and the proposed method, the experimental results are shown in Fig. 13 for qualitative comparison. In Fig. 13 (a), the first row is the hazy image 'House', the second row is the magnification of the red

rectangle in the source image, the third row is the hazy image 'Flag', and rows 4 and 5 correspond to the magnified images of the red rectangles in the 'Flag' image. Fig. 13 (b)–(g) are the experimental results of Kim's method, He's method, Tarel's method, Zhu's method and the proposed method, respectively. Compared with the hazy images, the visibility and contrast of each restored image are greatly improved, and all methods can achieve good dehazing effects for the corresponding hazy images. Nevertheless, the different methods obtain different degrees of improvement. For the 'House' image, the dehazing degree of Kim's method is the lowest from the visual perspective, whereas Tarel's method can realize deeper dehazing; however, it is accompanied by color distortion. In particular, the red wall is darker in the restored image. Relative to the above two methods, He's method, Zhu's method and the proposed method can achieve better results. However, from the magnified image in the second row, an obvious 'halo' artifact is shown in the image that used Zhu's method, and the overall effect of He's method is also not as good as the proposed method. For the 'Flag' image, the processing results of Kim's method, He's method, Zhu's method, and the proposed method are the most prominent in terms of visual effects. From the comparison of local details in the fifth row, Kim's method can obtain an outstanding result in the close-shot scenery with vivid color and high contrast. However, the effect of the long-shot scenery is not as good as in the other methods. He's and Zhu's methods can achieve good compromises in both close- and long-shot scenery. However, compared with the proposed method, the restored image of the proposed method has better sharpness, contrast, and color.

Then, the 'Mountain' image and 'NewYork2' images are used as the second group of experimental images by adopting Tan's method [21], Kopf's method [15], Fattal's method [22], Tarel's method [32], He's method [31], Kim's method [33], Meng's method [34], Zhu's method [37] and the proposed method for qualitative comparison, and the experimental results are shown in Fig. 14. These two images are classical and have long field depths. The reason that they were selected for comparison is that the different recovered images are easily download from the author's websites.

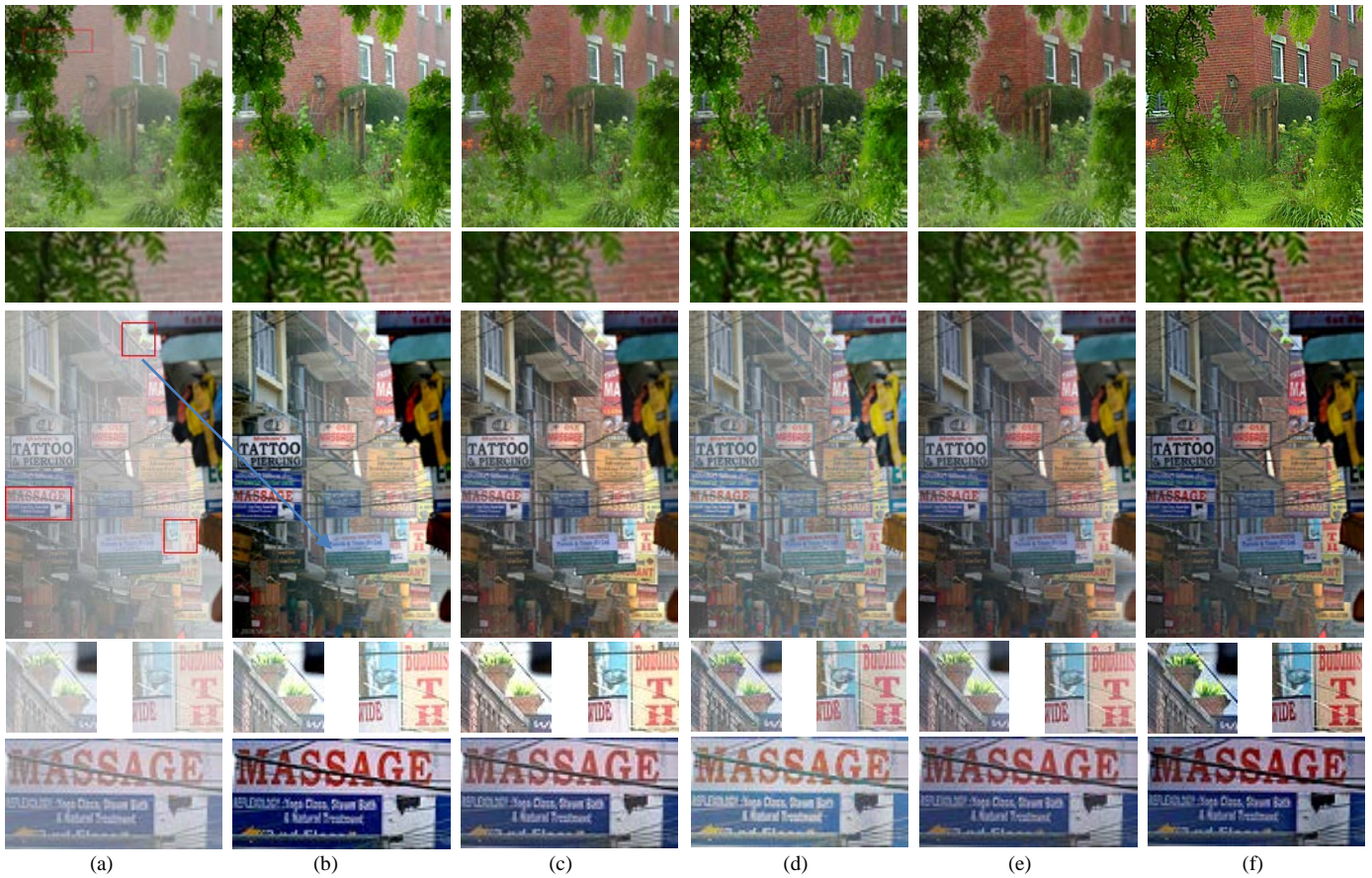


Fig. 13. Comparison with well-known image restoration methods (group 1). (a) Hazy image. (b) Kim's method[33]. (c) He's method[31]. (d) Tarel's method[32]. (e) Zhu's method[37]. (f) Proposed method.

Compared with the hazy image, the visibility and contrast of the two whole images are greatly improved from Fig. 14(b)-(j), and all of the above methods can relieve the influence of haze to some extent. Among those, Tan's method, He's method and Tarel's method have better dehazing effects on the hazy images, especially for the long-shot scenery. However, Tan's and Tarel's methods resulted in color shifting or over saturation, which appears as pseudo color in the haze-free image. Kopf's method and Fattal's method can better maintain the color of the

source image, but the overall effect lacks competitiveness. The results of Meng's method, Kim's method, Zhu's method and the proposed results are similar, and the tones are relatively consistent. However, the former three methods are not effective at processing the sharp-jump edges of the field depth in the scene. As shown by the amplified scenery images in the third row, the produced images of the proposed method are more clear, have a stronger sense of depth, and can overcome the color distortion problem in Tarel's method and Tan's method.

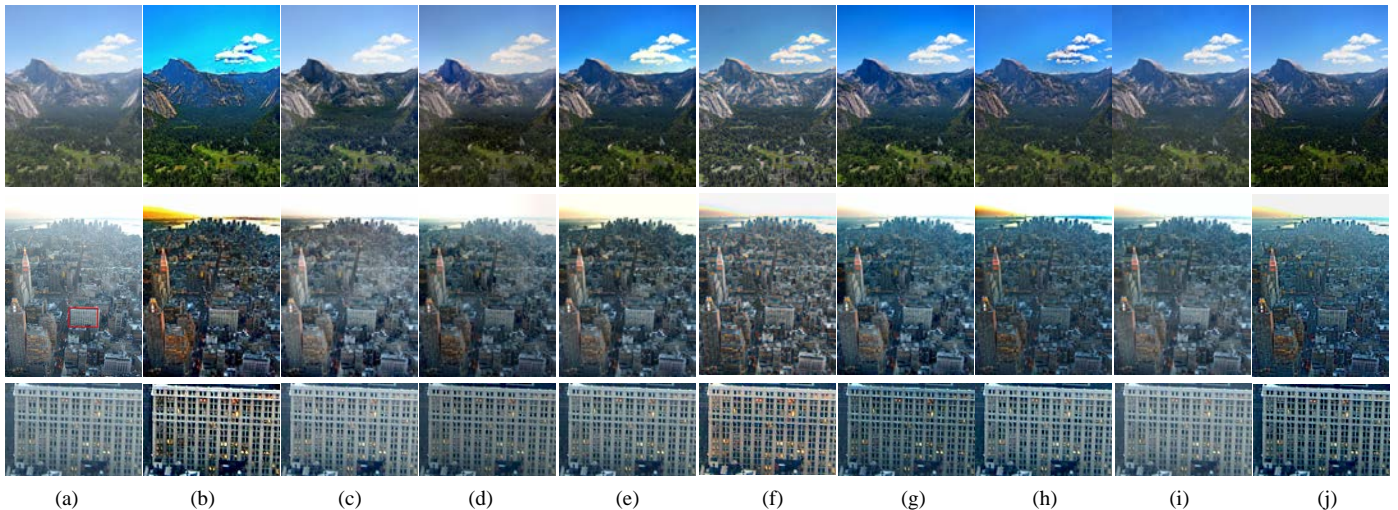


Fig. 14. Comparison with well-known image restoration methods (group 2). (a) Hazy image. (b) Tan's method[21]. (c) Kopf's method[15]. (d) Fattal's method[22]. (e) He's method[31]. (f) Tarel's method[32]. (g) Meng's method[34]. (h) Kim's method[33]. (i) Zhu's method[37]. (j) Proposed method.

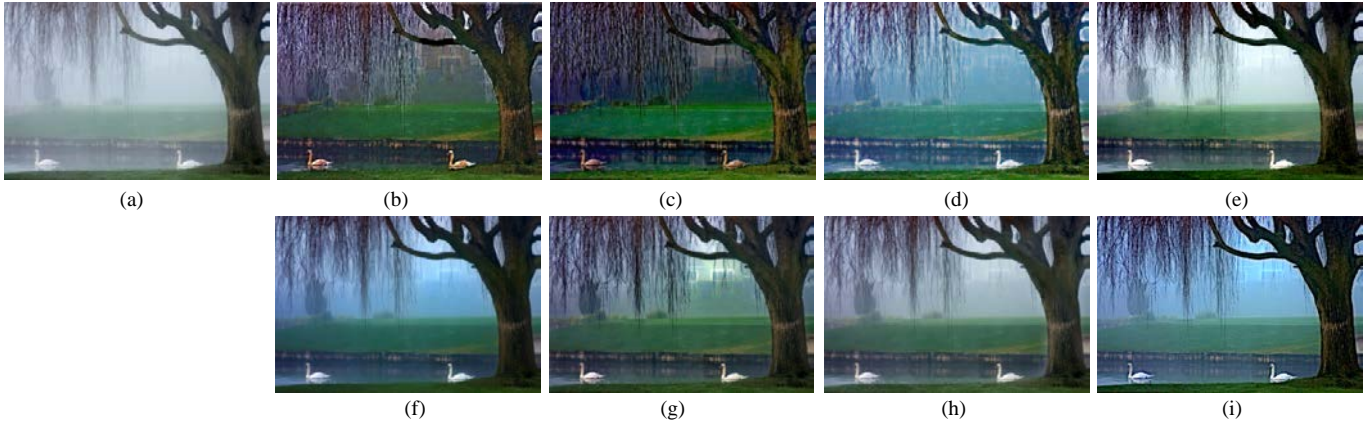


Fig. 15. Experimental results (group 1) of different methods on image 'Swan'. (a) Hazy image. (b) Tan's method [20]. (c) Nishino's method [24]. (d) Tarel's method [31]. (e) Kim's method [32]. (f) He's method [30]. (g) Meng's method [30]. (h) Zhu's method [36]. (i) Proposed method.

The analysis of Figs. 13 and 14 shows that the proposed method can recover haze-free images well from hazy images with different depths of field, different environments, and different illumination conditions. It shows outstanding performance compared to some of the well-known methods in terms of human visual perspective.

B. Objective Evaluation

Because subjective evaluation has inevitable bias, objective evaluation criteria are usually used to measure the effects of different methods [41,42]. For the objective evaluation of image dehazing, three aspects including mean square evaluation (MSE), peak signal-to-noise ratio (PSNR) and structural similarity (SSIM) [43] are employed for objective comparison. The expressions of MSE , $PSNR$ and $SSIM$ are as follows:

$$MSE = \frac{1}{M \times N} \sum_{i=0}^{M-1} \sum_{j=0}^{N-1} [f(i, j) - f'(i, j)]^2 \quad (18)$$

$$PSNR = 10 \lg \frac{f_{\max}^2}{MSE} \quad (19)$$

$$SSIM = F(l_c, c_c, s_c) \quad (20)$$

where M and N are the width and height of the image; $f(i, j)$ is the original image or reference image, which is obtained by changing the parameters of different methods manually and visually selecting the best one; $f'(i, j)$ is the restored image; f_{\max} is the largest gray value; and l_c , c_c , and s_c are the luminance comparison, contrast comparison and structure comparison, respectively.

For the three indexes, a smaller MSE, a larger PSNR, or a larger SSIM result in better image restoration. Due to the dimensional differences among the three data types, all of the data need to be normalized. The formula is expressed as:

$$y = \frac{(y_{\max} - y_{\min}) \times (x - x_{\min})}{x_{\max} - x_{\min}} + y_{\min} \quad (21)$$

where x_{\max} and x_{\min} are the maximum and minimum values of the data before normalization, y_{\max} and y_{\min} are the maximum and minimum of the normalized data, respectively. In this paper, $y_{\max} = 1$ and $y_{\min} = 0.6$.

In addition, because the MSE varies inversely with $SSIM$ and $PSNR$, a comprehensive performance parameter is expressed as:

$$Comp = SSIM + PSNR - MSE \quad (22)$$

where MSE , $PSNR$ and $SSIM$ are the normalized data.

The first group of experimental images is the 'Swan' image from Tan's personal website. The experimental image is shown in Fig. 15, where (b)-(i) are the restored images using Tan's method [21], Nishino's method [25], Tarel's method [32], Kim's method [33], He's method [31], Meng's method [34], Zhu's method [37], and the proposed method, respectively, and the quantitative experimental data are shown in Table 2. The proposed method achieved the best scores on the three performance indexes MSE , $PSNR$ and $SSIM$.

Tab. 2 Data for the different methods on the 'Swan' image

Index	Tan's method	Nishino's method	Tarel's method	Kim's method	He's method	Meng's method	Zhu's method	Proposed method
MSE	0.848	1.000	0.655	0.65	0.686	0.749	0.64	0.600
$PSNR$	0.668	0.600	0.849	0.859	0.802	0.736	0.878	1.000
$SSIM$	0.702	0.600	0.835	0.887	0.945	0.847	0.985	1.000
$Comp$	0.522	0.200	1.029	1.096	1.061	0.834	1.223	1.400

The second groups of experimental images is named 'Cones'. The experimental results in Fig. 16 from left to right are the hazy image, followed by the images restored using Fattal's method [22], Nishino's method [25], Meng's method [34], He's method [26,31], Kim's method [33], Zhu's method [37], and proposed method, respectively.

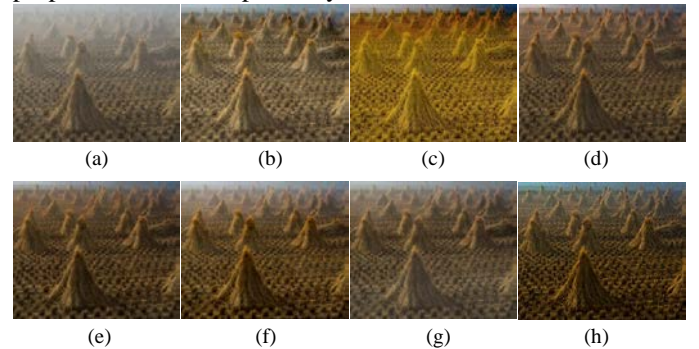


Fig. 16. Experimental results (group 2) of different methods on 'Cones'. (a) Hazy image. (b) [22] method. (c) [25] method. (d) [34] method. (e) [26] method. (f) [33] method. (g) [37] method. (h) Proposed method.

Fig. 17 is the corresponding data graph of ‘Cones’, where the columns in red, green, blue, and black represents the *MSE*, *PSNR*, *SSIM* and *Comp* data, respectively. In Fig. 17, *MSE*, *PSNR*, *SSIM* and *Comp* all have the best results. This fully shows that our method can obtain not only high color fidelity but also get better image structure from hazy images. In addition, it has outstanding comparativeness to the other methods.

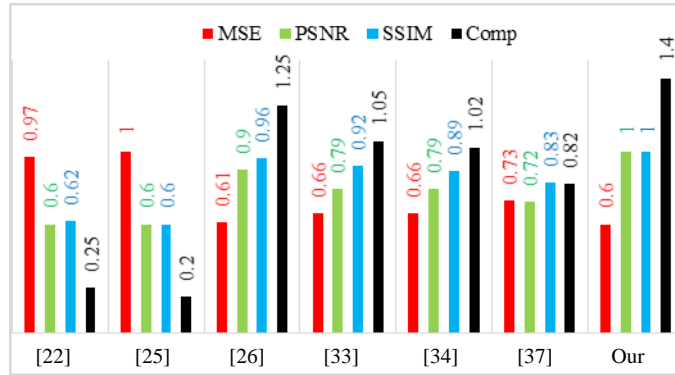


Fig. 17. Experimental data histograms for the image ‘Cones’

The other group’s experiments are also performed to compare the proposed method with the other methods. The source images are from different scenes and have different depth characteristics. Fig. 18 shows the images, and Table 3 shows the comparison of the experimental results based on the *Comp* item.



Fig. 18. Source images for the experiments

Tab. 3 Data from the different methods on Fig. 18 images

Index	Tarel’s method	Kim’s method	He’s method	Meng’s method	Zhu’s method	Proposed method
Image 1	0.200	1.062	1.379	1.243	1.242	1.261
Image 2	0.220	1.243	0.694	1.246	0.614	1.400
Image 3	0.200	0.911	0.997	0.534	0.621	1.400
Image 4	1.085	0.880	1.359	0.200	1.033	1.235
Image 5	0.775	0.949	1.097	1.004	0.200	1.400
Image 6	0.303	0.548	0.832	0.767	0.200	1.400
Image 7	0.325	0.938	0.546	0.493	0.297	1.400
Image 8	0.200	0.842	0.464	0.796	0.816	1.400
Image 9	0.200	0.956	1.124	1.007	0.518	1.400

Table 3 shows that, for the nine images, the proposed method can achieve the best value on seven images. For the other two images, it has the second best value, which fully shows that our method can obtain not only high color fidelity but also obtain better image structure from hazy images. In addition, it has outstanding comparativeness to the other methods.

C. Computational Complexity

To verify the speed advantage of the proposed method,

various images with different sizes were tested, and the running times are compared with He’s method [26,31], Tarel’s method [32], Meng’s method [34] and Zhu’s method [37]. Here, He1 is the DCP+soft matting method [26], and He2 is the DCP+guided filtering method [31]. The window size used to calculate DCP is set to 15×15 pixels. To ensure the fairness of the comparison, all programs of the different methods are run in the MATLAB environment, the atmospheric light is set to the same value in initialization, the program code is mainly running for transmission map estimation, and image restoration is performed five times to find the average time. From Table 4, it is evident that the He1 method has the lowest operational efficiency on a single image, where the symbol ‘-’ stands for ‘out of memory.’ This result is mainly because the soft matting is a problem when solving large sparse linear equations with high computational complexity. It can only be used to calculate finite size images.

Tab. 4 Running time of the different methods (Unit: s)

Resolution (pixels)	He1[26] method	Tarel[32] method	Meng[34] method	He2[31] method	Zhu[37] method	Proposed method
600×400	21.763	7.656	1.243	<u>0.584</u>	0.887	0.048
800×600	47.926	23.147	2.290	<u>1.205</u>	1.699	0.075
1024×768	83.776	56.873	3.796	<u>3.766</u>	2.675	0.115
1600×1200	–	303.153	9.380	7.765	<u>6.546</u>	0.237
2048×1536	–	721.632	15.885	14.561	<u>10.732</u>	0.362
3200×2400	–	4138.646	35.536	31.329	<u>27.363</u>	0.728
4096×3072	–	–	65.211	52.434	<u>44.352</u>	1.133

Tarel’s method was optimized using a median filter; however, as the size of the image increased, the computational complexity rapidly increased. In the He2 method [31], the guided filter was used to replace the soft matting in the He1 method [26]. The running time was greatly improved after the optimization, and it showed that it can quickly process a large image. The efficiencies of Meng’s method and Zhu’s method are similar to that of the He2 method. Zhu’s method used the linear model and guided filter; as the image size increased, the running speed remains fast. Compared to the above methods, the proposed method has outstanding running efficiency. From a 600×400 pixel image to a 4096×3072 pixel image, the number of pixels increases approximately 50 times; however, the time consumption is only 23 times longer. It takes only 1.1 s to complete the operation on a 4096×3072 pixel image, which is only 1/40 of the time of Zhu’s method. Thus, it is obvious that our proposed method has the absolute advantage of running time over the other methods.

To compare the increasing speed of the computing time for each method when the image size increased, the relative time approach was employed for comparison. Assuming that the processing time of the minimum size image is t_1 , the relative operation time is expressed as:

$$T_r = t_n / t_1 \quad (23)$$

In which n is the image index, which increases with of the size of test images. The relative time curves of Meng’s method [34], the He2 method [31], Zhu’s method [37] and the proposed method are shown in Fig. 19. For each size, ten different images are selected for the test, and each image will be calculate ten times. All the computational times of the same size images will be averaged.

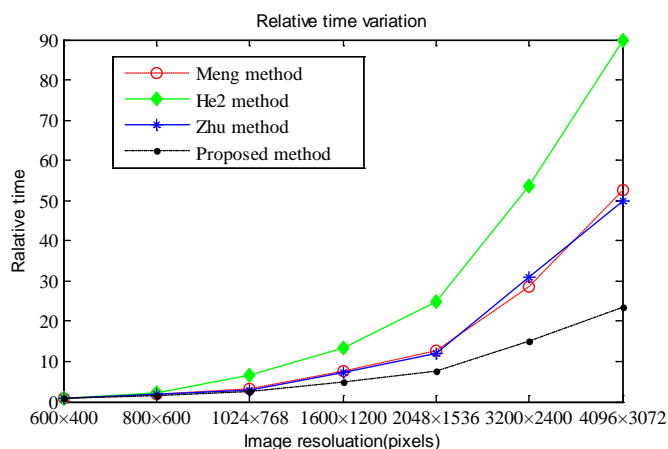


Fig. 19. Curves of relative time changing with the image size

As shown in Fig. 19, as the image size increases, the relative time of the various methods all gradually increase. The He2 method has the maximum slope, and its changing rate is the fastest; Zhu's method and Meng's method have basically the same changing trend, while the proposed method is the slowest. This is mainly because the linear model was adopted for estimating the transmission map, and the main operation time was derived from the optimization with the Gaussian filter. To sum up, our proposed method has a highly efficient implementation.

The proposed method only needs approximately 48 ms to complete single image dehazing on a 600×400 pixel image in the MATLAB operating environment. Thus, it can meet the needs of 20 frames per second in a real-time system. As the image size increases, the running time slowly increases, which is suitable for the dehazing of large images.

V. CONCLUSIONS

In this paper, under the assumption that the smallest color channel of a hazy image has a linear relationship with that of its haze-free image, a simple and efficient method of transmission map estimation was proposed. The weakening strategy was designed to solve the problem of brightness distortion in some areas, and Gaussian blurring was adopted to refine the transmission map. Furthermore, to adapt to the position of the sky area and obtain the atmospheric light, an additional channel method was presented based on a quad-tree subdivision by using the ratio of average grays and gradients in the region for accurate estimation.

In this method, the estimation of the transmission map is based on a linear model that includes only linear operations without any exponential operations or sample training. Therefore, it is easy to realize and has less computational complexity. The main operation time of this algorithm was derived from the transmission optimization with a Gaussian filter, while the fast filter makes the Gaussian filtering work quickly. Therefore, for large image sizes or video from hazy conditions, it can not only improve the dehazing effect but also guarantee the computing speed. The experimental results show that the method can avoid the phenomena of over saturation and halo effects, and the restoration of details and color is very natural, which can not only meet the visual requirements in

subjective terms, but it has great advantages in the implementation efficiency. Moreover, it can be used for image feature analysis and recognition in real-time outdoor systems. The main problem in the algorithm is that the color of the restored image may darken with increased dehazing level, although some image processing methods can be used for correction. A method of adaptively determining the correction parameters or avoiding this phenomenon still needs to be further improved and perfected in the future.

REFERENCES

- [1] J. Wang, W. Wang, R. Wang, and W. Gao, "CSPPS: an adaptive pooling method for image classification," *IEEE Trans. Multimedia*, vol. 18, no. 6, pp. 1000–1010, Jun. 2016.
- [2] S. C. Huang, B. H. Chen, and Y. J. Cheng, "An efficient visibility enhancement algorithm for road scenes captured by intelligent transportation systems," *IEEE Trans. Intell. Transp. Syst.*, vol. 15, no. 5, pp. 2321–2332, May 2014.
- [3] M. Saini, X. Wang, P. Atrey, and M. Kankanhalli, "Adaptive workload equalization in multi-camera surveillance systems," *IEEE Trans. Multimedia*, vol. 14, no. 3, pp. 555–562, Mar. 2012.
- [4] X. Pan, F. Xie, Z. Jiang, and J. Yin, "Haze removal for a single remote sensing image based on deformed haze imaging model," *IEEE Signal Process. Lett.*, vol. 22, no. 10, pp. 1806–1810, Oct. 2015.
- [5] M. Negru, S. Nedevschi, and R. I. Peter, "Exponential contrast restoration in fog conditions for driving assistance," *IEEE Trans. Intell. Transp. Syst.*, vol. 16, no. 4, pp. 2257–2268, Apr. 2015.
- [6] J. Y. Chiang and Y. C. Chen, "Underwater image enhancement by wavelength compensation and dehazing," *IEEE Trans. Image Process.*, vol. 21, no. 4, pp. 1756–1769, Apr. 2012.
- [7] T. K. Kim, J. K. Paik, and B. S. Kang, "Contrast enhancement system using spatially adaptive histogram equalization with temporal filtering," *IEEE Trans. Consum. Electron.*, vol. 44, no. 1, pp. 82–86, Feb. 1998.
- [8] H. Xu, G. Zhai, X. Wu, and X. Yang, "Generalized equalization model for image enhancement," *IEEE Trans. Multimedia*, vol. 16, no. 1, pp. 68–82, Jan. 2014.
- [9] T. J. Cooper and F. A. Baqai, "Analysis and extensions of the Frankle-McCann Retinex algorithm," *J. Electron. Imag.*, vol. 13, no. 1, pp. 85–92, Jan. 2004.
- [10] M. J. Seow and V. K. Asari, "Ratio rule and homomorphic filter for enhancement of digital colour image," *Neurocomputing*, vol. 69, no. 7, pp. 954–958, Jul. 2006.
- [11] S. Dippel, M. Stahl, R. Wiemker, and T. Blaffert, "Multiscale contrast enhancement for radiographies: Laplacian pyramid versus fast wavelet transform," *IEEE Trans. Med. Imag.*, vol. 21, no. 4, pp. 343–353, Apr. 2002.
- [12] J. P. Oakley and B. L. Satherley, "Improving image quality in poor visibility conditions using models using model for degradation," *IEEE Trans. Image Process.*, vol. 7, no. 2, pp. 167–179, Feb. 1998.
- [13] S. G. Narasimhan and S. K. Nayar, "Interactive (de) weathering of an image using physical models," in *Proc. IEEE Workshop Color Photometric Methods Comput. Vis.*, vol. 6, France, 2003, pp. 1–8.
- [14] N. Hautiere, J. P. Tarel, and D. Aubert, "Towards fog-free in-vehicle vision systems through contrast restoration," in *Proc. IEEE Conf. Comput. Vis. Pattern Recognit.*, MN, USA, Jun. 2007, pp. 1–8.
- [15] J. Kopf et al., "Deep photo: model-based photograph enhancement and viewing," *ACM Trans. Graph.*, vol. 27, no. 5, pp. 116, May 2008.
- [16] Y. Y. Schechner, S. G. Narasimhan, and S. K. Nayar, "Instant dehazing of images using polarization," in *Proc. IEEE Conf. Comput. Vis. Pattern Recognit.*, HI, USA, Dec. 2001, pp. 325–332.
- [17] S. Shwartz, E. Namer, and Y. Y. Schechner, "Blind haze separation," in *Proc. IEEE Conf. Comput. Vis. Pattern Recognit.*, Jun. 2006, pp. 1984–1991.
- [18] S. K. Nayar and S. G. Narasimhan, "Vision in bad weather," in *Proc. IEEE Int. Conf. Comput. Vis.*, vol. 2, Sep. 1999, pp. 820–827.
- [19] S. G. Narasimhan and S. K. Nayar, "Chromatic framework for vision in bad weather," in *Proc. IEEE Conf. Comput. Vis. Pattern Recognit.*, Jun. 2000, pp. 598–605.
- [20] S. G. Narasimhan and S. K. Nayar, "Contrast restoration of weather degraded images," *IEEE Trans. Pattern Anal. Mach. Intell.*, vol. 25, no. 6, pp. 713–724, Jun. 2003.
- [21] R. T. Tan, "Visibility in bad weather from a single image," in *Proc. IEEE Conf. Comput. Vis. Pattern Recognit.*, AK, USA, Jun. 2008, pp. 1–8.

- [22] R. Fattal, "Single image dehazing," *ACM Trans. Graph.*, vol. 27, no. 3, pp. 1–9, Aug. 2008.
- [23] R. Fattal, "Dehazing using color-lines," *ACM Trans. Graph.*, vol. 34, no. 1, pp. 1–14, Dec. 2014.
- [24] L. Kratz and K. Nishino, "Factorizing scene albedo and depth from a single foggy image," in *Proc. IEEE Int. Conf. Comput. Vis.*, Sep. 2009, pp. 1701–1708.
- [25] K. Nishino, L. Kratz, and S. Lombardi, "Bayesian defogging," *Int. J. Comput. Vis.*, vol. 98, no. 3, pp. 263–278, Jul. 2012.
- [26] K. He, J. Sun, and X. Tang, "Single image haze removal using dark channel prior," *IEEE Trans. Pattern Anal. Mach. Intell.*, vol. 33, no. 12, pp. 2341–2353, Dec. 2011.
- [27] J. Yu, D. Li, and Q. Liao, "Physics-based fast single image fog removal," *Acta Autom. Sinica*, vol. 37, no. 2, pp. 143–149, Feb. 2011.
- [28] K. B. Gibson, D. T. Vo, and T. Q. Nguyen, "An investigation of dehazing effects on image and video coding," *IEEE Trans. Image Process.*, vol. 21, no. 2, pp. 662–673, Feb. 2012.
- [29] M. Ding and R. Tong, "Efficient dark channel based image dehazing using quadrees," *Sci. China Inf. Sci.*, vol. 56, no. 9, pp. 1–9, Sep. 2013.
- [30] Y. H. Shiao, H. Y. Yang, P. Y. Chen, and Y. Z. Chuang, "Hardware implementation of a fast and efficient haze removal method," *IEEE Trans. Circuits Syst. Video Technol.*, vol. 23, no. 8, pp. 1369–1374, Aug. 2013.
- [31] K. He, J. Sun, and X. Tang, "Guided image filtering," *IEEE Trans. Pattern Anal. Mach. Intell.*, vol. 35, no. 6, pp. 1397–1409, Jun. 2013.
- [32] J. P. Tarel and N. Hautiere, "Fast visibility restoration from a single color or gray level image," in *Proc. IEEE Int. Conf. Comput. Vis.*, Kyoto, Japan, Sep. 2009, pp. 2201–2208.
- [33] J. H. Kim, W. D. Jang, J. Y. Sim, and C. S. Kim, "Optimized contrast enhancement for real-time image and video dehazing," *J. Visual Commun. Image Represent.*, vol. 24, no. 3, pp. 410–425, Apr. 2013.
- [34] G. Meng, Y. Wang, J. Duan, S. Xiang, and C. Pan, "Efficient image dehazing with boundary constraint and contextual regularization," in *Proc. IEEE Int. Conf. Comput. Vis.*, Sydney, Australia, Dec. 2013, pp. 617–624.
- [35] C. O. Ancuti and C. Ancuti, "Single image dehazing by multi-scale fusion," *IEEE Trans. Image Process.*, vol. 22, no. 8, pp. 3271–3282, Aug. 2013.
- [36] Z. Ma, J. Wen, C. Zhang, Q. Liu, and D. Yan, "An effective fusion defogging approach for single sea fog image," *Neurocomputing*, vol. 173, pp. 1257–1267, 2016.
- [37] Q. Zhu, J. Mai, and L. Shao, "A fast single image haze removal algorithm using color attenuation prior," *IEEE Trans. Image Process.*, vol. 24, no. 11, pp. 3522–3533, Nov. 2015.
- [38] W. Wang, X. Yuan, X. Wu, Y. Liu, and S. Ghanbarzadeh, "An efficient method for image dehazing," in *Proc. IEEE Int. Conf. Image Process.*, Phoenix, AZ, USA, Sep. 2016, pp. 2241–2245.
- [39] E. J. McCartney, "Optics of the atmosphere: scattering by molecules and particles," New York, John Wiley and Sons, Inc., 1976, pp. 1–5.
- [40] M. Sulami, I. Glatzer, R. Fattal, and M. Werman, "Automatic recovery of the atmospheric light in hazy images," in *Proc. IEEE Int. Conf. Comput. Photogr.*, Santa Clara, CA, USA, May 2014, pp. 1–11.
- [41] X. Tang, W. Luo, and X. Wang, "Content-based photo quality assessment," *IEEE Trans. Multimedia*, vol. 15, no. 8, pp. 1930–1943, Aug. 2013.
- [42] K. Gu, G. Zhai, X. Yang, and W. Zhang, "Using free energy principle for blind image quality assessment," *IEEE Trans. Multimedia*, vol. 17, no. 1, pp. 50–63, Jan. 2015.
- [43] Z. Wang, A. C. Bovik, H. R. Sheikh, and E. P. Simoncelli, "Image quality assessment: from error visibility to structural similarity," *IEEE Trans. Image Process.*, vol. 13, no. 4, pp. 600–612, Apr. 2004.



Wencheng Wang received the Ph.D. degrees in pattern recognition and intelligent system from the Shandong university, Jinan, in 2011. And now he is an associate professor of College of Information and Control Engineering in Weifang University. From 2006 to 2007, he was visiting scholar at Qingdao University of Science and Technology, and now he is a visiting scholar in

University of North Texas and engaging in the research of computer vision and automatic detection technology, especially

on image dehazing. His group has published and authored more than 30 papers on academic journals and conference, four book chapters and 5 patents. His main research interests include computer vision, pattern recognition, and intelligent computing.



Xiaohui Yuan received B.S. degree in Electrical Engineering from Hefei University of Technology, China in 1996 and Ph.D. degree in Computer Science from Tulane University in 2004. After his graduation, he worked at the National Institutes of Health on medical imaging and analysis till 2006. He joined the University of North Texas (UNT) as

an Assistant Professor in 2006 and was promoted to Associate Professor with tenure in 2012. His research interests include computer vision, data mining, machine learning, and artificial intelligence. He served as PI and co-PI in projects supported by Air Force Lab, National Science Foundation (NSF), Texas Advanced Research Program, Oak Ridge Associated Universities, and UNT. His research findings are reported in over 70 peer-reviewed papers. Dr. Yuan is a recipient of Ralph E. Powe Junior Faculty Enhancement award in 2008 and the Air Force Summer Faculty Fellowship in 2011, 2012, and 2013. He served in the editorial board of several international journals and served as session chairs in many conferences, as well as panel reviewer for funding agencies including NSF, NIH, and Louisiana Board of Regent's Research Competitiveness program. He is a member of IEEE and SPIE.



Xiaojin Wu received the PhD degree in 2011. And now he is working in College of Information and Control Engineering, Weifang University. He has published and authored more than 10 papers on academic journals and conferences. His main research interests include computer vision, intelligent system and image processing.



Yunlong Liu was born in Rizhao City, Shandong Province, PR China, in 1982. He received his Ph.D degree in Marine sciences from Ocean University of China in 2012. Since 2012, he has been working as a lecturer in the College of Information and Control Engineering at Weifang University, PR China. He has published and authored more than 20 papers on academic journals and conferences. His

research interests include variable structure control, intelligent control, singular systems and information processing